Chapter 6

Chapter 6

Influence of plasmonic nanostructure geometry on a host semiconductor and optimization of key parameters for enhanced photocatalytic efficiency

In the preceding two chapters, two distinct types of photocatalysts were developed, each incorporating Ag nanostructures to exploit LSPR for enhanced photocatalytic performance. The study revealed that DET and PIRET were the notable mechanisms through which LSPR enabled enhancement. Notably, the efficiency of LSPR is strongly influenced by the size and shape of the metal nanostructures supporting it. Therefore, to gain deeper insight into the influence of size and shape on photocatalytic performance, Ag@TiO_2 photocatalysts with three distinct Ag nanostructure morphologies were synthesized and investigated in this chapter. Specifically, spherical, cubic, and bulbous branched Ag nanostructures were prepared using chemical reduction methods. Each morphology exhibited a unique plasmonic resonance spectrum, highlighting the shape-dependent nature of LSPR. The shape-based effect in plasmonic photocatalysis have been studied by successfully incorporating these Ag metal nanoparticles onto TiO_2 semiconductor photocatalyst. The degradation of MB was performed using each of these photocatalysts and compared. Additionally, the optimization of Ag loading was achieved by evaluating the photocatalytic activity of samples prepared with varying Ag concentrations. The calcination temperature of the host semiconductor was also systematically varied to determine the optimal thermal treatment condition for enhanced photocatalytic efficiency. The analysis results demonstrate that a particular shape of Ag with suitable size, loading amount, and calcination temperature, leads to the highest activity of the photocatalyst. The work presented in this chapter addresses some key objectives of this thesis, focusing on the influence of plasmonic nanostructure morphology on photocatalytic activity and the optimization of host semiconductor and co-catalyst parameters for maximum efficiency.

6.1. Introduction

It is already established that the performance of a plasmonic photocatalyst depends on the plasmonic counterpart, the compatibility of the plasmonic material, and the host semiconductor. The plasmonic behaviour of noble metals such as Ag and Au has been

extensively studied, and it was reported that the different sizes and shapes of the same metallic nanoparticle can strongly affect the pattern of the plasmonic resonance spectra [1-4]. As particle size increases beyond the quantum confinement regime, the plasmonic resonance peak exhibits a red shift [5]. This is primarily due to the ease of separating the associated charges further in larger particles, which consequently lowers the frequency of the collective oscillation of electrons, resulting in a red shift of the resonance peak. This behaviour has been observed in nanospheres as their diameter increases and in Ag nanocubes as their edge length increases [6, 7]. The shape of the particle also affects the plasmonic response. It has been observed that the lower the symmetry of the nanoparticle, the greater the number of resonances supported by the particle. A nanosphere exhibits one single resonance peak, while a nanocube and nanorod exhibit two resonance peaks because of their unique symmetry [2]. A sphere is isotropic, while a nanorod or nanocube is anisotropic. Thus, two types of resonances—longitudinal and transverse polarisation, have been observed in anisotropic particle such as nanorods [8]. If the size of a particle is larger and the shape supports even more resonances, then broad plasmonic spectra are observed over a range of wavelengths [9]. For example, nanostars with branching features show broad plasmonic resonance absorption. Additionally, the intensity of the plasmonic resonance peak has been observed to be influenced by the strength of the dipole formed within a structure; therefore, symmetries that allow large charge separation to facilitate greater dipole formation tend to exhibit higher peak intensities compared to symmetries that do not possess such characteristics [2]. Moreover, the presence of sharp corners or edges facilitates effective charge separation, leading to a reduction in the restoring force required for the oscillation of the charges in plasmonic resonance. Consequently, this induces a notable shift of the plasmonic resonance peak towards longer wavelengths [2, 10]. When comparing two nanostructures of similar sizes, the presence of sharp corners in one and rounded structures in the other causes a significant difference in their plasmonic resonance behavior. In particular, the nanostructure with sharp corners shows a red-shift in the resonance peaks in comparison to the primary dipole resonances observed in the rounded structures. Furthermore, the sharp edges and tips of nanoparticles have a tremendous effect on the local electric field intensity generated by the plasmonic resonance. These features have been reported to increase the local

electrical field in the vicinity of the particle by a factor of around 1000, known as the lightning rod effect [3,9]. This can enhance the photocatalytic performance of the plasmonic photocatalyst by aiding in charge separation and generation through well-known mechanisms like local electromagnetic field enhancement (LEMF) and plasmon-induced resonant energy transfer (PIRET) [11].

Thus a plasmonic photocatalyst can truly benefit from its plasmonic counterpart if it possess optimized size and shape, along with the good compatibility with the semiconductor. In this study, different shapes of Ag have been synthesized and their photocatalytic influences are evaluated. For this, TiO_2 was chosen as the host semiconductor which has good compatibility with Ag due to the high DOS of TiO_2 and suitable Fermi level of Ag [12]. Three shapes of Ag—spherical, cubical, and bulbous branching structures—were successfully prepared and incorporated into TiO_2. The photocatalytic performance was evaluated by measuring the degradation of MB, and each sample was characterized with XRD, SEM and TEM to verify shape incorporation. Among the various synthesized shapes, the cubical Ag particle proved to be the best plasmonic counterpart for TiO_2.

6.2. Experimental section

6.2.1. Materials and methods

Titanium isopropoxide [$Ti(OCH(CH_3)_2)_4$] was purchased from Alfa Aesar. Silver nitrate [$AgNO_3$], 2-propanol [$(CH_3)_2CHOH$], Ascorbic acid [$C_6H_8O_6$], and nitric acid [HNO_3] were acquired from Merck, India. Polyvinyl Pyrolidone [PVP] was supplied by Himedia Laboratories Pvt. Ltd, India. Tri-sodium Citrate Dihydrate [$C_6H_5Na_3O_7.2H_2O$], and Sodium Borohydrate [$NaBH_4$] were purchased from Merck Life Science Private Limited.

For the synthesis of spherical Ag nanoparticles (Ag(S)), first 100 mL of 0.25 mM $AgNO_3$ solution was first prepared using distilled water. An equimolar amount (0.25 mM) of trisodium citrate dihydrate was then added. After obtaining a clear solution, 1 mL of 10 mM $NaBH_4$ was slowly introduced under continuous stirring using a micropipette, resulting in the formation of a clear yellow colloidal solution.

For the synthesis of Ag nanocubes (Ag(C)), 0.0075 g of $AgNO_3$ was dissolved in 50 mL of distilled water. Subsequently, 7 mL of the previously prepared spherical Ag nanoparticle solution was added as a seed solution. After thorough mixing, 4 mL of

0.16 mM PVP solution was introduced, followed by the slow addition of 0.5 mL of 100 mM L-ascorbic acid under continuous stirring. The solution gradually developed a bluish-purple color.

Again, bulbous branched Ag nanostructures (Ag(B)) were prepared by mixing equal volumes (10 mL each) of 4.6 mM L-ascorbic acid and $AgNO_3$ solution. The reaction yielded a precipitate, which was subsequently collected by centrifugation.

Next, the $Ag@TiO_2$ photocatalyst incorporating bulbous branched Ag nanostructures was synthesized using the following procedure. Ti (IV) isopropoxide (8.88 mL) was mixed with isopropanol in a 1:10 volume ratio under continuous stirring. After 30 minutes, 0.01 g of branched Ag was added, and stirring was continued for another 30 minutes. Subsequently, 1 mL of 1 M HNO_3 was introduced, followed 20 minutes later by the dropwise addition of 200 µL of distilled water. The mixture was stirred continuously for 24 hours and then left undisturbed for another 24 hours to allow aging. The resulting solid was dried at 80-100 ºC, ground into a fine powder, and calcined at 600 ºC for 2 hours.

For the incorporation of Ag nanospheres or nanocubes into TiO_2 to prepare $Ag@TiO_2$ photocatalysts, the following procedure was employed. Ti (IV) isopropoxide (4 mL) was mixed with isopropanol in a 1:10 volume ratio and stirred for 30 minutes. Subsequently, 1 mL of 1 M HNO_3 was added, and stirring was continued for another 30 minutes. Then, 500 µL of distilled water was added dropwise, followed by an additional 30 minutes of stirring. After this, 10 mL of Ag nanosphere or nanocube solution was gradually introduced (1 mL at a time) under continuous stirring. The subsequent steps of aging, drying, and calcination were carried out in the same manner to obtain the final product.

6.2.2. Characterization

The photocatalysts were characterized using a range of analytical techniques, including XRD, UV-visible DRS, SEM, TEM, Raman spectroscopy, photoluminescence, and XPS. Instrumentation details for each technique are provided in Chapter 2. The photocatalytic performance was assessed through the degradation of MB dye, following the methodology outlined in Chapter 2.

6.3. Results and discussion

6.3.1. Photocatalytic performance optimization coupled with XRD study

The XRD patterns of the Ag@TiO_2 photocatalysts prepared with spherical, cubical and bulbous Ag nanoparticles, designated as Ag@TiO_2(S), Ag@TiO_2(C), and Ag@TiO_2(B), respectively, are shown in Figure 6.1(a). The diffraction spectra of Ag@TiO_2(S) and Ag@TiO_2(B) show both the anatase and rutile peaks.

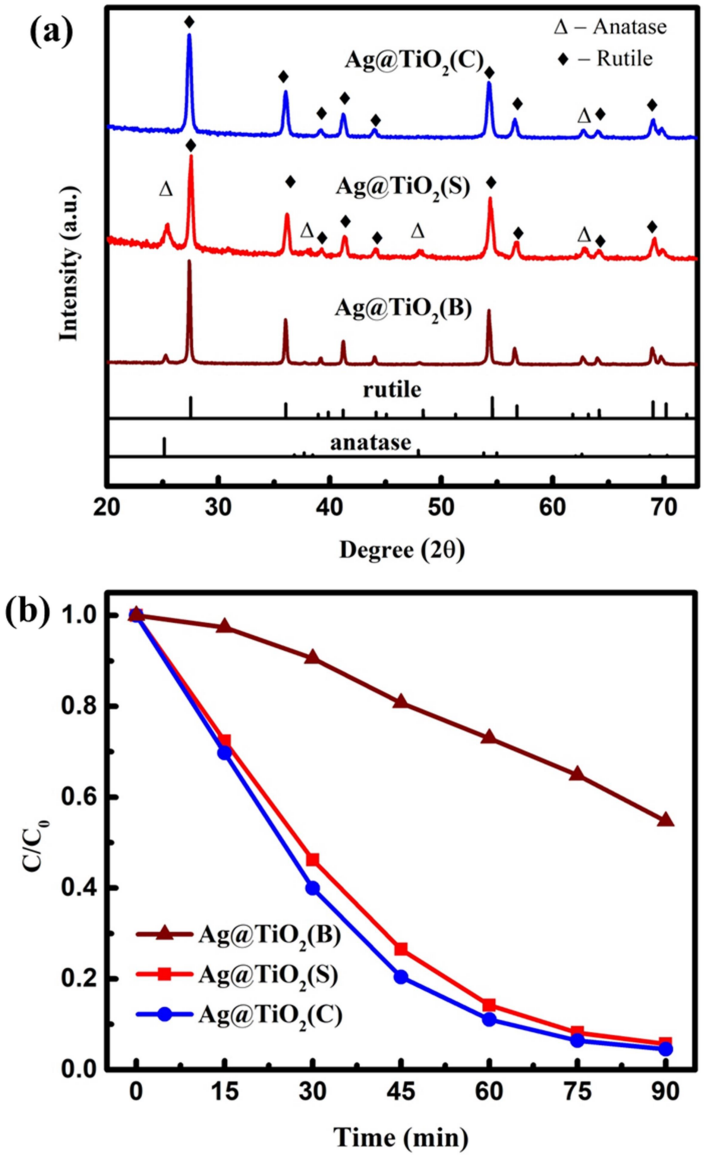

Figure 6.1. (a) XRD spectra of Ag@TiO_2 calcined at 600 ºC prepared with different Ag shapes and (b) photocatalytic degradation profile (C/C_0 vs. time) of MB using the samples under visible light.

The anatase peaks are located at 25.3º, 37.8º, 48.1º, and 62.8º (PDF no 89-4921) with (101), (004), (200), and (204) as their corresponding crystal planes, while the rutile peaks are observed at 27.4º, 36.1º, 39.2º, 41.3º, 44.1º, 54.4º, 56.7º, 64.2º, and 69.1º (PDF no 89-4920) having crystal planes as (110). (101), (200), (111), (210), (211), (220), (310), and (301), respectively. However, the XRD pattern of Ag@TiO_2(C) exhibits a dominant rutile phase (PDF no 89-4920), with only a single weak diffraction peak corresponding to the anatase phase at 62.8°. The rutile peaks of Ag@TiO_2(C) are located at the same positions as those observed in Ag@TiO_2(S) and Ag@TiO_2(B). No distinct peaks corresponding to Ag were observed, likely due to the relatively low concentration of silver compared to TiO_2 in the samples.

The photocatalytic performance of the samples Ag@TiO_2(S), Ag@TiO_2(C), and Ag@TiO_2(B) have been evaluated, and are shown in Figures 6.1(b) and 6.2. Figure 6.1(b) shows the degradation profile of (C/C_0 vs. time) of MB under visible light. Figure 6.2(a) shows the ln C/C_0 vs. time plot to determine the rate constant. It was observed that Ag@TiO_2(C) shows the highest activity among the prepared samples. Figure 6.2(b) illustrates the degradation percentage of photocatalysts in a bar diagram. Table 6.1 presents the rate constant values of the photocatalysts. Ag@TiO_2(C) shows 1.1 and 6 times higher activity than Ag@TiO_2(S) and Ag@TiO_2(B) respectively. Moreover, Ag@TiO_2(C) shows 35-times higher activity than the pristine TiO_2 whose activity was reported in Chapter 4. Due to its superior performance, Ag@TiO_2(C) was further optimized by varying the loading of cubic Ag and the thermal treatment conditions.

To optimize the loading of cubic Ag nanoparticles, two variants of Ag@TiO_2(C) photocatalysts were additionally synthesized using 5 mL and 20 mL of cubic Ag solution. The resulting powders were calcined at 600 ºC, and labeled as Ag@TiO_2(C5) and Ag@TiO_2(C20), respectively. For ease of comparison, the original sample prepared with 10 mL of cubic Ag solution was designated as Ag@TiO_2(C10). Figure 6.3 presents the XRD patterns of Ag@TiO_2(C5), Ag@TiO_2(C10), and Ag@TiO_2(C20). The results show that Ag@TiO_2(C5) and Ag@TiO_2(C20) have similar 2θ peak positions, except for the peaks at 39.2° and 64.19°, which correspond to the rutile phase, and are observed in Ag@TiO_2(C5) and Ag@TiO_2(C10) but absent in Ag@TiO_2(C20). The matching XRD peak positions of Ag@TiO_2(C5) and Ag@TiO_2(C20) are observed at 25.3º, 37.0º, 37.8º, 38.6º, 48.1º, 53.8º, 55.1º, and 62.8º (PDF no 89-4921) attributed to the anatase phase

with (101), (103), (004), (112), (200), (105), (211), and (204) as their corresponding crystal planes. Similarly, the matching rutile peaks of Ag@TiO_2(C5) and Ag@TiO_2(C20) are located at 27.4º, 36.1º, 41.3º, 44.1º, 54.4º, 56.7º, 64.2º, and 69.1º (PDF no 89-4920), which are observed in Ag@TiO_2(C10) as well. As already established, XRD spectra of Ag@TiO_2(C10) shows only one single anatase peak located at 62.8º. Moreover, the intensity of the main anatase peak at 25.3º is stronger in Ag@TiO_2(C20) than in Ag@TiO_2(C5), and is completely missing in Ag@TiO_2(C10).

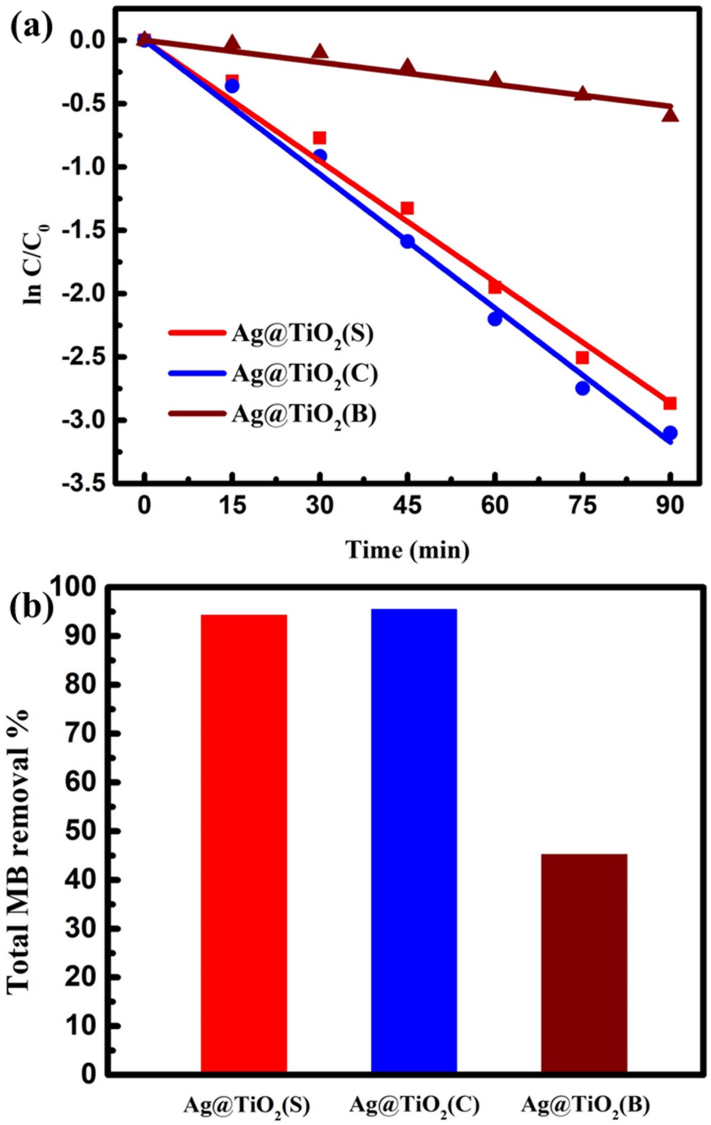

Figure 6.2. (a) ln C/C_0 vs. time plot to determine the rate constant of the MB degradation using Ag@TiO_2 calcined at 600 ºC prepared with different Ag shapes, (b) bar chart representing the dye degradation capabilities of the photocatalysts.

Table 6.1. Rate of MB degradation using Ag@TiO_2 photocatalysts calcined at 600 ºC prepared with different shapes.

Photocatalyst	Rate constant (min^{-1})	Regression coefficient
Ag@TiO_2(S)	0.0318	0.99
Ag@TiO_2(C)	0.0352	0.99
Ag@TiO_2(B)	0.0058	0.96

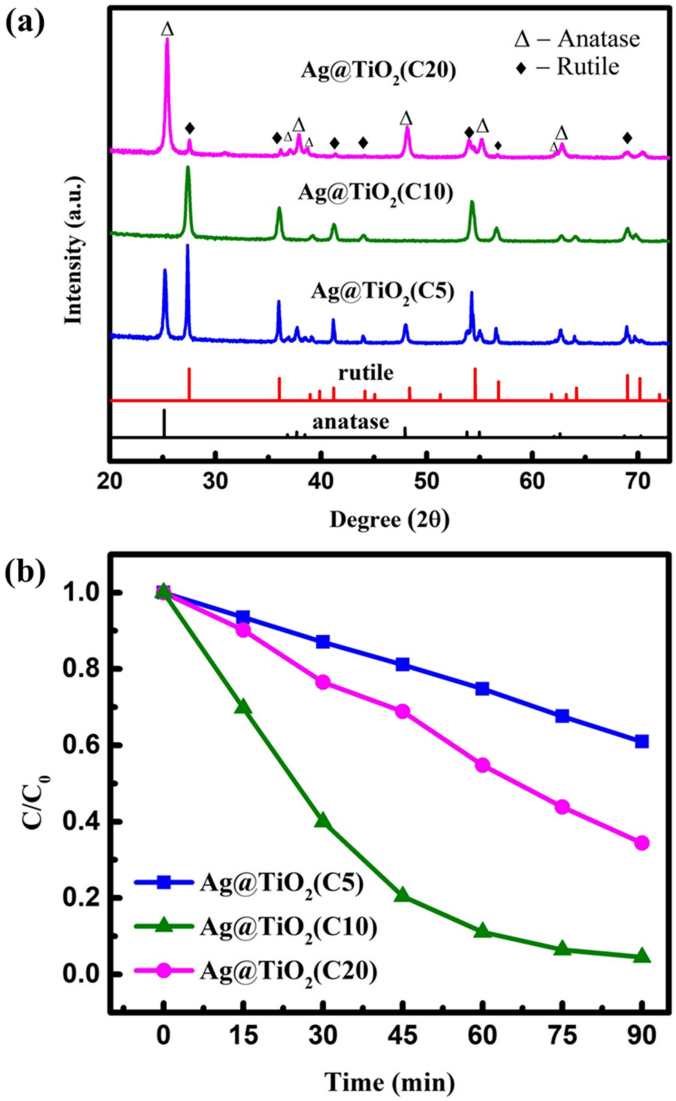

Figure 6.3. (a) XRD spectra of Ag@TiO_2 calcined at 600 ºC prepared with different Ag concentration and (b) photocatalytic degradation profile (C/C_0 vs. time) of MB using the samples under visible light.

This suggests a mixed anatase-rutile phase composition, with Ag@TiO_2(C10) being rutile-dominant, Ag@TiO_2(C20) anatase-rich, and Ag@TiO_2(C5) exhibiting a balanced mixture of both phases. The photocatalytic performance of the samples Ag@TiO_2(C5), Ag@TiO_2(C10), and Ag@TiO_2(C20) are shown in Figure 6.3(b) and 6.4(a-b). Figure 6.3(b) shows the degradation profile of (C/C_0 vs. time) of MB under visible light. Figure 6.4(a) shows the ln C/C_0 vs. time plot to determine the rate constant. Figure 6.4(b) illustrates the degradation percentage of photocatalysts in the bar diagram. It was observed that the Ag@TiO_2(C10) shows highest activity among the prepared samples.

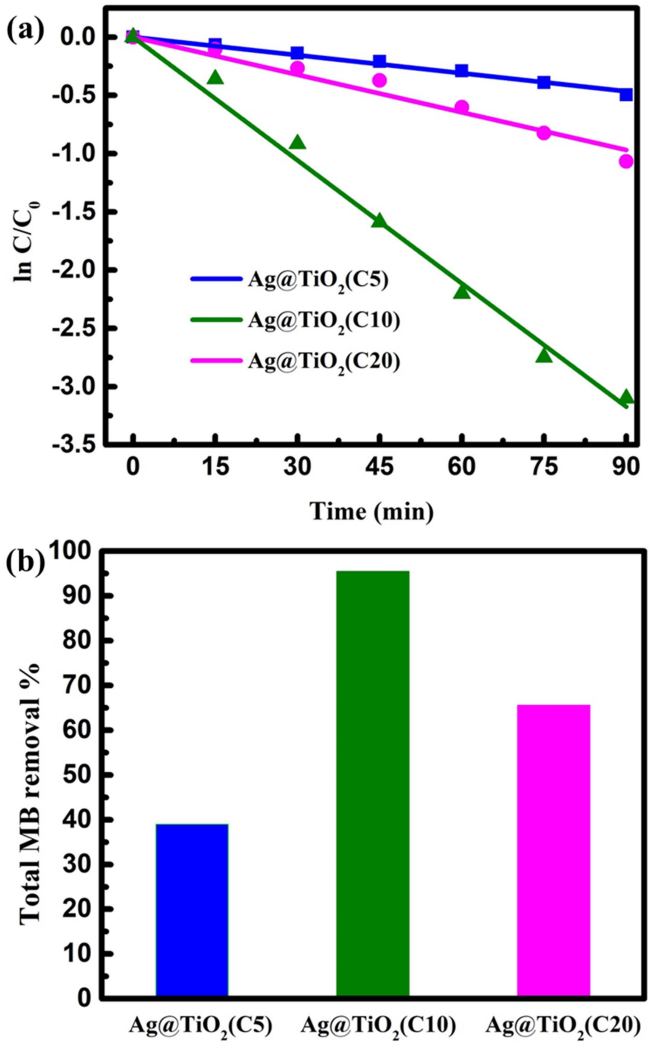

Figure 6.4. (a) ln C/C_0 vs. time plot to determine the rate constant of the MB degradation using Ag@TiO_2 calcined at 600 ºC prepared with different Ag loading, (b) bar chart representing the dye degradation capabilities of the photocatalysts.

The rate constant values, summarized in Table 6.2, indicate that Ag@TiO_2(C10) achieved 6.9 and 3.2 times higher activity than Ag@TiO_2(C5) and Ag@TiO_2(C20), respectively. Based on these results, 10 mL Ag loading is identified as the optimal concentration, and the Ag@TiO_2(C10) photocatalyst was subsequently selected for further optimization of the calcination temperature.

To optimize the calcination temperature, the most active Ag@TiO_2(C) photocatalyst was further calcined at 400 ºC, 500 ºC, and 700 ºC, in addition to the previously analyzed sample Ag@TiO_2(C10) at 600 ºC. A comparison of the XRD patterns, shown in Figure 6.5(a) reveals that Ag@TiO_2(C10) calcined at 600 ºC and 700 ºC exhibit similar diffraction features, characterized by multiple rutile peaks and a single anatase peak at 62.8°. In contrast, Ag@TiO_2(C10) calcined at 400 ºC displays broad, diffuse humps centred around typical anatase peak positions, suggesting an amorphous structure in the early stages of crystallization. This transition is further confirmed by the well-defined anatase peaks observed in the sample calcined at 500 ºC, which appear at positions matching the broad features seen in the 400 ºC sample. The positions of the anatase peaks are 25.35º, 37.8º, 38.6º, 48.1º, 53.8º, 55.1º, and 62.8º (PDF no 89-4921) with (101), (004), (112), (200), (105), (211), and (204) as their corresponding crystal planes. The photoactivity of these photocatalysts calcined at various temperatures have been compared, and are shown in Figures 6.5(b) and 6.6(a-b). Figure 6.5(b) shows the degradation profile of (C/C_0 vs. time) of MB under visible light. Figure 6.6(a) shows the ln C/C_0 vs. time plot to determine the rate constant. Figure 6.6(b) illustrates the degradation percentage of photocatalysts in bar diagram. It was observed that Ag@TiO_2(C10) at 600 ºC outperforms all the samples prepared at other temperatures. The rate constant of the photocatalysts are shown in Table 6.3.

To gain a better perspective on which specific parameter most significantly enhances photocatalytic activity, a comparative analysis was conducted. Figure 6.7(a) presents the XRD patterns of all Ag@TiO_2 photocatalysts exhibiting rutile phases only. The XRD patterns of Ag@TiO_2(S), Ag@TiO_2(B), Ag@TiO_2(C5), Ag@TiO_2(C10) and Ag@TiO_2(C20) each possessing rutile phase are presented in Figure 6.7(a). For most samples, the rutile phase appears only after calcination at 700 ºC, except for Ag@TiO_2(C10), which already shows rutile characteristics at 600 ºC. The corresponding photocatalytic performances are shown in Figures 6.7(b) and 6.8(a-b).

Table 6.2. Rate of MB degradation using Ag@TiO_2 photocatalysts calcined at 600 ºC prepared with different concentration of cubical Ag nanoparticles

Photocatalyst	Rate constant ((min^{-1}))	Regression coefficient
Ag@TiO_2(C5)	0.0051	0.99
Ag@TiO_2(C10)	0.0352	0.99
Ag@TiO_2(C20)	0.0107	0.98

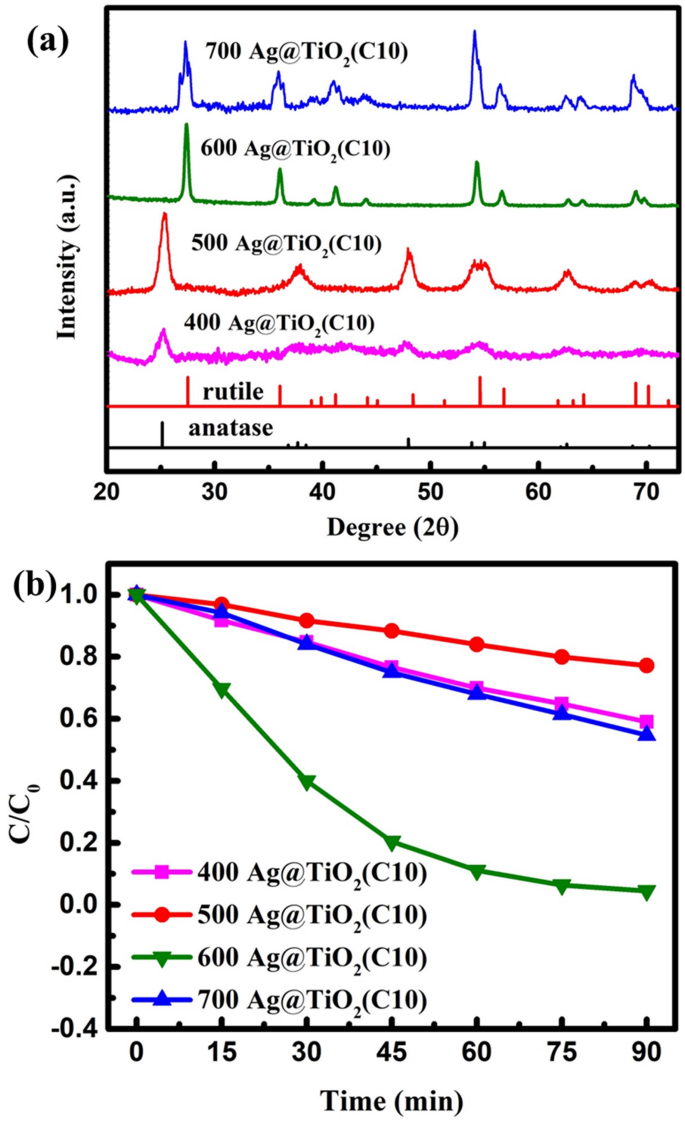

Figure 6.5. (a) XRD spectra of Ag@TiO_2 with 10 mL cubical Ag loading, calcined at different temperatures and (b) photocatalytic degradation profile (C/C_0 vs. time) of MB using the samples under visible light.

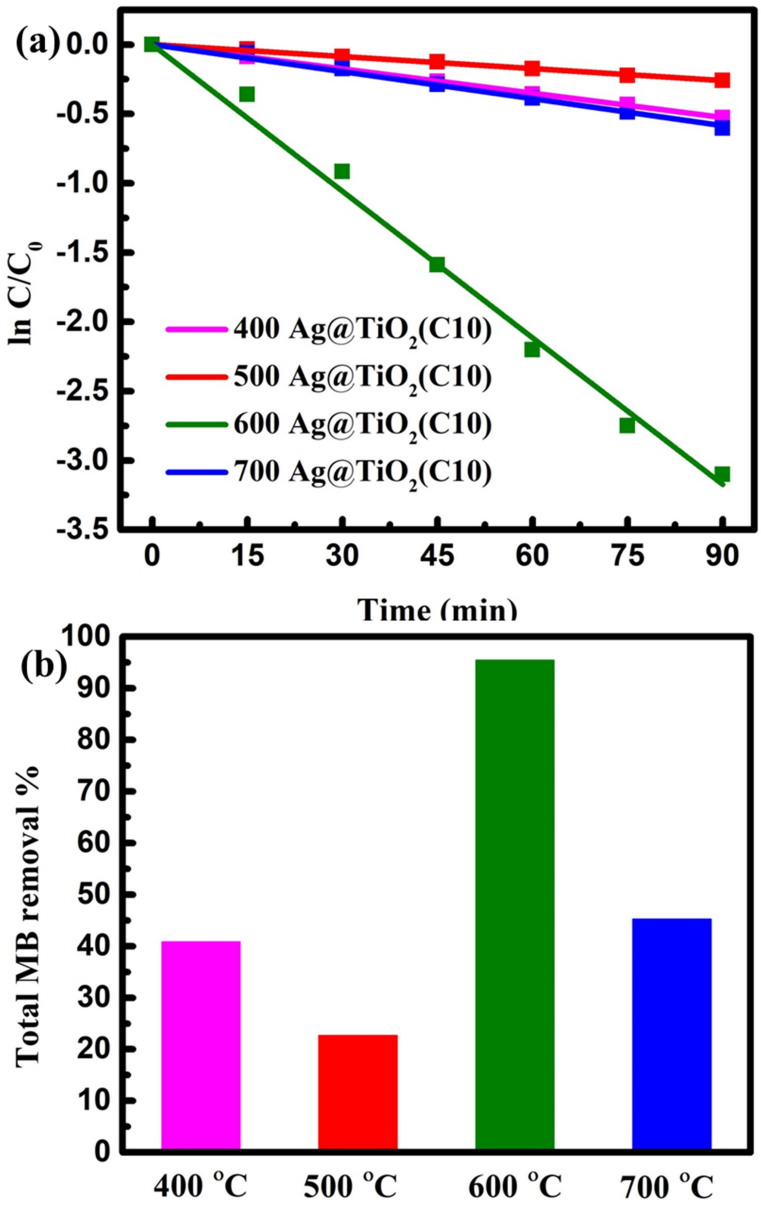

Figure 6.6. (a) ln C/C_0 vs. time plot to determine the rate constant of the MB degradation using Ag@TiO_2(C10), calcined at different temperatures, (b) bar chart representing the dye degradation capabilities of the photocatalysts.

Table 6.3. Rate of MB degradation using Ag@TiO_2 photocatalysts with 10 mL cubical Ag loading, calcined at different temperatures

Photocatalyst	Rate constant (min^{-1})	Regression coefficient
400 Ag@TiO_2(C10)	0.0058	0.99
500 Ag@TiO_2(C10)	0.0029	0.99

600 Ag@TiO_2(C10)	0.0352	0.99
700 Ag@TiO_2(C10)	0.0065	0.99

As summarized in Table 6.4, Ag@TiO_2(C10) consistently demonstrates the highest rate constant and photocatalytic efficiency. These results confirm rutile-phase Ag@TiO_2(C10) as the most optimized photocatalyst among all rutile-phase candidates.

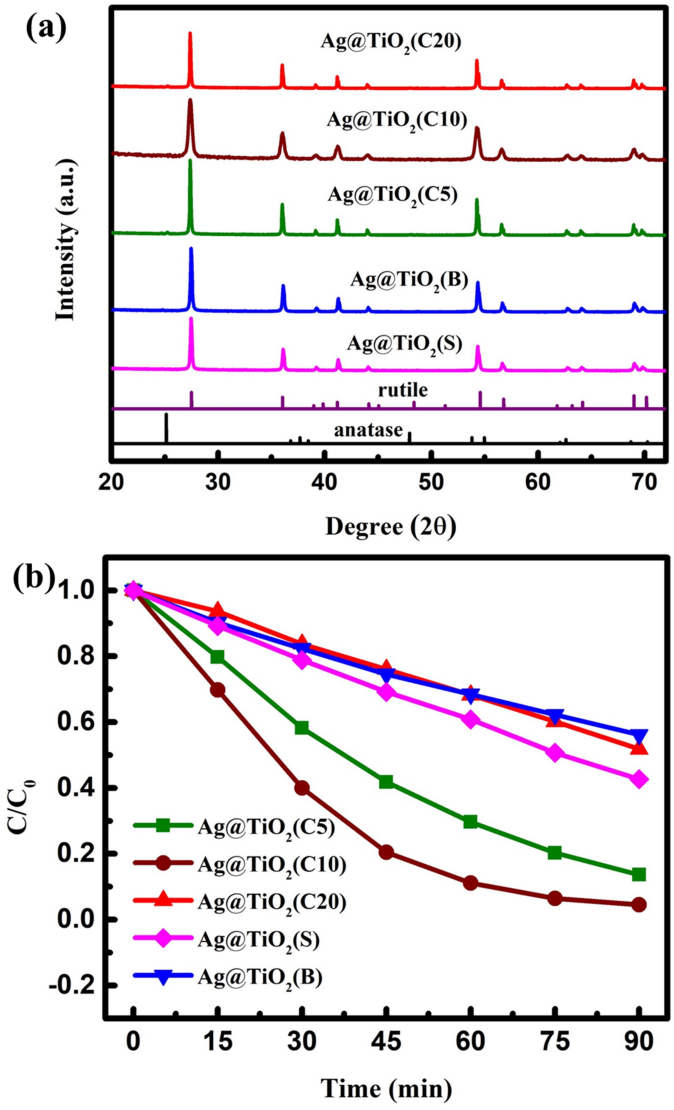

Figure 6.7. (a) X-ray diffraction spectra of different Ag@TiO_2 photocatalysts having rutile phases and (b) photocatalytic degradation profile (C/C_0 vs. time) of MB using the samples under visible light.

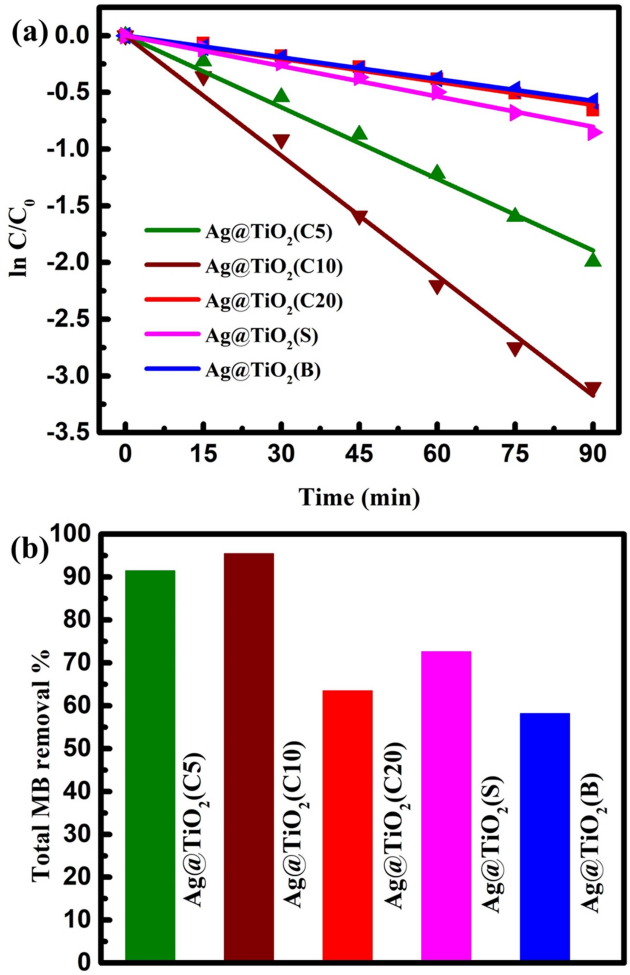

Figure 6.8. (a) ln C/C_0 vs. time plot to determine the rate constant of the MB degradation using different Ag@TiO_2 photocatalysts having rutile phases, (b) bar chart representing the dye degradation capabilities of the photocatalysts.

Table 6.4. Rate of MB degradation using different Ag@TiO_2 photocatalysts having rutile phases

Photocatalyst	Rate constant (min^{-1})	Regression coefficient
rutile Ag@TiO_2(C5)	0.02	0.99
rutile Ag@TiO_2(C10)	0.0352	0.98
rutile Ag@TiO_2(C20)	0.0067	0.98
rutile Ag@TiO_2(S)	0.0089	0.99
rutile Ag@TiO_2(B)	0.0063	0.99

6.3.2. UV-visible absorbance and DRS characterization

The UV-vis absorbance spectra of various shaped Ag particles and the UV-vis DRS spectra of corresponding Ag@TiO_2 photocatalyst prepared using each of the spherical, cubical, and branched shaped Ag particles are shown in Figure 6.9(a). As shown in Figure 6.9(a), the spectra of spherical Ag nanoparticles has one intense peak located at about 390 nm, while the cubical Ag shows two peaks located at 288 nm and 417 nm. The moderate broadening of the peak for spherical Ag suggests the presence of particles with a distribution of diameters, indicating slight size polydispersity. The two peaks observed in the spectrum of cubical Ag nanoparticles arise from shape anisotropy, which enables distinct plasmonic resonances along different crystallographic directions of the cube, resulting in absorption at two separate wavelengths. The one at 417 nm is of relatively higher intensity than that at 288 nm. In contrast, the bulbous branched Ag nanoparticles exhibit no distinct peaks but rather a continuous rise in absorbance from 321 nm to beyond 700 nm. This broad spectral response is attributed to their large size and complex branched morphology, which may support multiple plasmon modes, resulting in the broadening of the overall absorption spectrum.

The UV-vis DRS spectra of the Ag@TiO_2 photocatalysts, each synthesized using spherical, cubical, and bulbous Ag nanoparticles, closely resemble the absorption profile of pure TiO_2, as shown in Figure 6.9(a), but exhibit slight variations. These differences can be attributed to the superposition of the absorption features of their respective Ag counterparts. A noticeably steeper rise in the spectrum of Ag@TiO_2(S) is detected starting around 425 nm. Meanwhile, Ag@TiO_2(C) exhibits a more gradual rise in absorbance, aligning closely with the wavelength range of 525-425 nm, where its metallic co-catalyst, cubical Ag, shows broad plasmonic absorption peaking around 418 nm and tapering off toward 700 nm. This clearly indicates that the absorption onset in the spectra of Ag@TiO_2(S) and Ag@TiO_2(C) is strongly influenced by the position and nature of the plasmonic absorption peaks of their respective Ag nanoparticles. In particular, since the most intense peak of spherical Ag appears around 390 nm, the absorption spectrum of Ag@TiO_2(S) also reaches its peak intensity close to this wavelength. Similarly, the spectrum of Ag@TiO_2(B) shows its highest absorbance around 360 nm, precisely where its corresponding branched Ag nanoparticles exhibit a marked increase in absorbance. This absorbance continues to rise across the visible

spectrum, resulting in broad spectral coverage. Additionally, a broad hump observed in the 550-700 nm range in the Ag@TiO_2(B) spectrum aligns with the rising absorbance profile of the branched Ag particles, indicating strong spectral overlap.

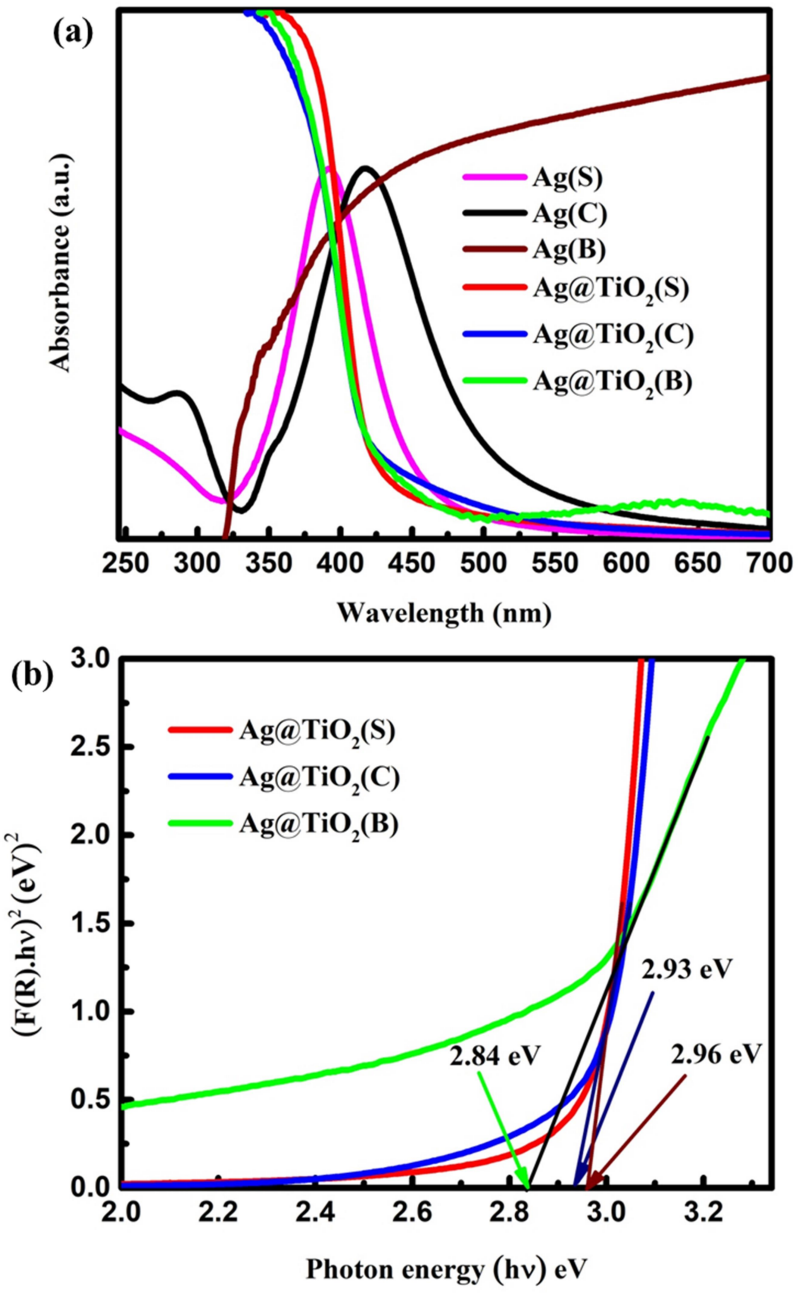

Figure 6.9. (a) UV-vis DRS of Ag@TiO_2(S), Ag@TiO_2(C), Ag@TiO_2(B); and UV-vis absorbance spectra of spherical, cubical and bulbous Ag, (b) bandgap determination of the photocatalysts.

Figure 6.9(b) presents the Tauc plots of the Ag@TiO_2 photocatalysts, derived using the Kubelka-Munk function to estimate their optical bandgaps. The calculated bandgap energies were found to be 2.96 eV for Ag@TiO_2(S), 2.93 eV for Ag@TiO_2(C), and 2.84 eV for Ag@TiO_2(B). These values indicate a slight narrowing of the bandgap compared to pure rutile TiO_2, which typically exhibits a bandgap of around 3.02 eV as reported in chapter 4.

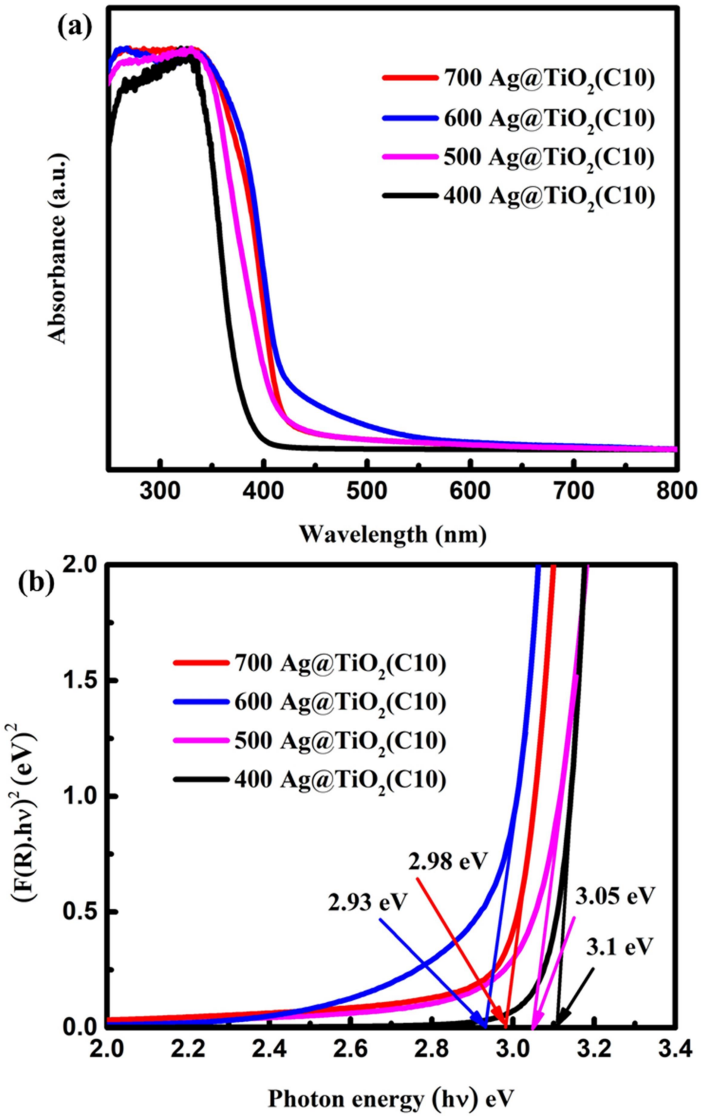

Figure 6.10. (a) UV-DRS of Ag@TiO_2(C) calcined at various temperatures, (b) bandgap determination using Tauc plot.

The UV-DRS spectra of Ag@TiO_2(C) photocatalysts calcined at different temperatures are shown in Figure 6.10(a). Notably, the sample calcined at 600 ºC

exhibits a distinctive absorption profile, characterized by the most gradual onset of absorption beginning around 550 nm. The corresponding Tauc plots, used for estimating the optical bandgaps, are presented in Figure 6.10(b). Among all Ag@TiO_2(C) samples, Ag@TiO_2(C) calcined at 600 ºC displays the lowest bandgap energy of 2.93 eV. In comparison, the bandgaps of Ag@TiO_2(C) calcined at 400 ºC, 500 ºC, and 700 ºC were found to be 3.10 eV, 3.05 eV, and 2.98 eV, respectively. This trend highlights the influence of calcination temperature on the optical properties of the photocatalysts, with 600 ºC emerging as the optimal temperature for bandgap narrowing and enhanced visible light absorption.

6.3.3. Structural and morphological analysis

The different shapes of synthesized Ag nanoparticles, intended for evaluating the shape-dependent effects on the photocatalytic activity of Ag@TiO_2, were confirmed through TEM imaging. Figure 6.11(a-d) presents the TEM images of spherical Ag nanoparticles at different magnifications, clearly verifying the successful formation of spherical Ag nanostructures.

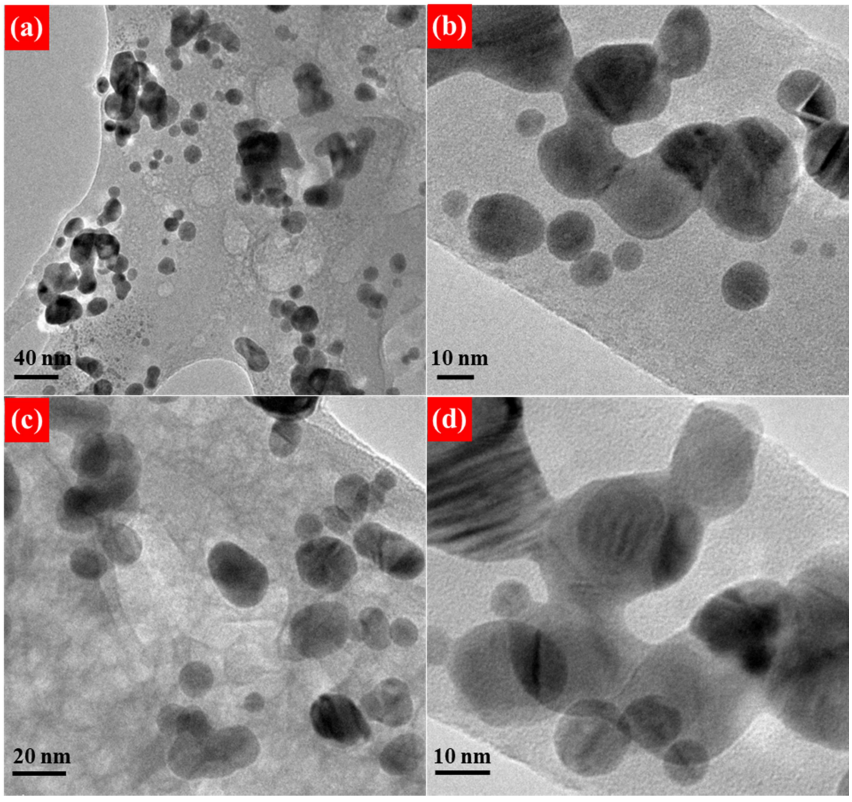

Figure 6.11. (a-d) TEM images of Ag(S).

The particles appear well-defined and uniformly distributed, with diameters ranging from approximately 5 nm to 25 nm.

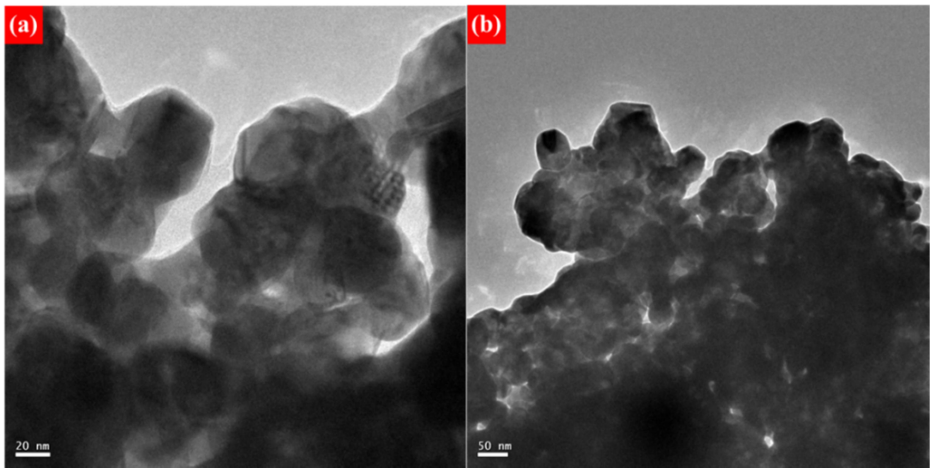

Figure 6.12. (a-b) TEM images of Ag(C).

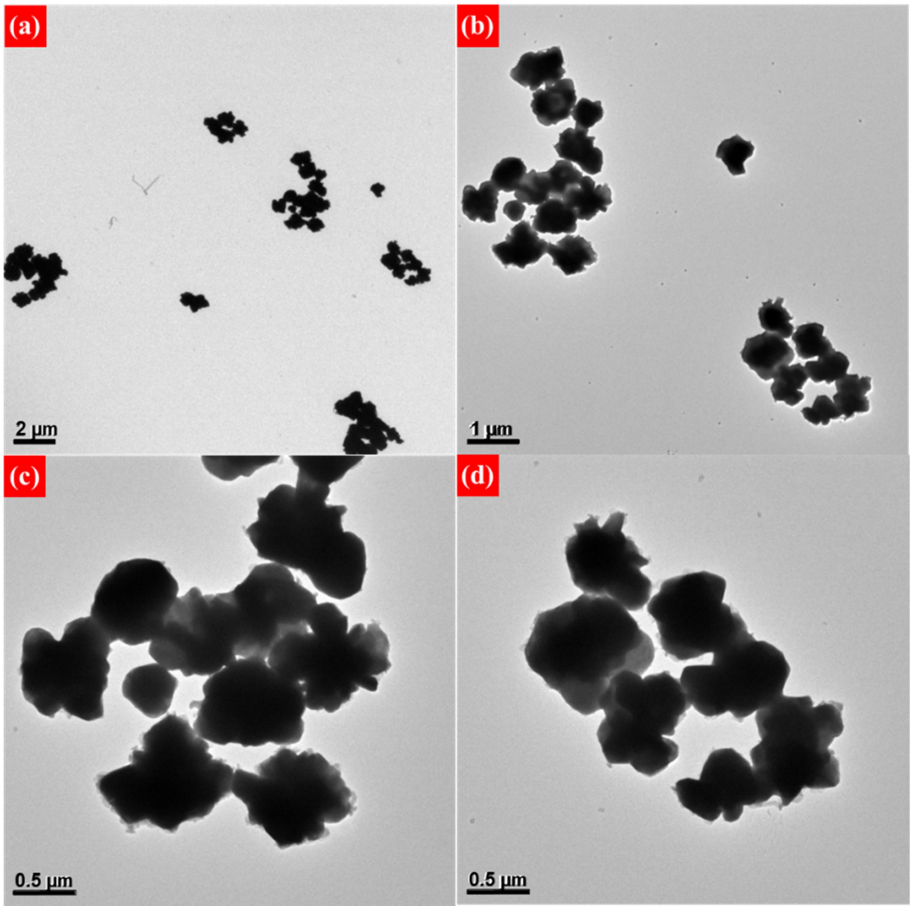

Figure 6.13. (a-d) TEM images of Ag(B).

Similarly, Figure 6.12(a-b) displays the TEM images of Ag nanoparticles with cubical morphology, confirming the successful formation of well-defined Ag cubes. The sizes of these cubical nanoparticles were found to be ranging between 20 nm and 70 nm. Furthermore, the distinctive morphology of bulbous branched Ag nanoparticles is evident in the TEM images shown in Figure 6.13(a-d), captured at different magnifications. These branched structures, characterized by irregular protrusions and larger overall dimensions, exhibit sizes ranging from approximately 0.2 μm to 0.9 μm, indicating their substantially larger and more complex geometry compared to the spherical and cubical structure. The TEM images presented in Figure 6.14(a-d) confirm the successful incorporation of spherical Ag nanoparticles into the Ag@TiO_2(S) photocatalyst. Figure 6.14(a) highlights the spherical Ag particles prior to their integration, with several particles outlined to emphasize their morphology. Their corresponding diameters are also labeled, providing a comparative view of particle size distribution. These images collectively validate the retention of spherical geometry in the composite structure, as indicated in Figure 6.14(b-d). The sizes of the spherical Ag nanoparticles observed in the TEM images of Ag@TiO_2(S) fall within the same range (15-18 nm) as those measured from the TEM image of the separately synthesized spherical Ag nanoparticles shown in Figure 6.14(a), indicating that the morphology and size are well-preserved during the photocatalyst synthesis. The incorporation of Ag into the TiO_2 matrix is further confirmed by the HRTEM image, shown in Figure 6.15(a) and the SAED pattern in Figure 6.15(b), of Ag@TiO_2(S) calcined at 600 ºC. In the HRTEM image, interplanar spacings of 0.32 nm and 0.23 nm are observed, which correspond to the (110) plane of rutile TiO_2 and the (111) plane of metallic Ag, respectively. Additionally, the SAED pattern exhibits diffraction rings indexed to the (111) plane of Ag and the (204) plane of anatase TiO_2, further corroborating the successful formation of the Ag@TiO_2(S) composite with both TiO_2 polymorphs and metallic Ag.

Similarly, the successful incorporation of cubical Ag nanoparticles into the TiO_2 matrix is confirmed through the TEM images shown in Figure 6.16(a-d). Figure 6.16(a) displays clearly outlined and labeled cubical Ag nanoparticles with sizes ranging from 20 to 70 nm. The dimensions of the cubical particles observed within the TiO_2 matrix in Figure 6.16(b-d) are consistent with those of the separately synthesized Ag cubes. This

provides a credible evidence that the cubical morphology of Ag is retained in the Ag@TiO_2(C) photocatalyst.

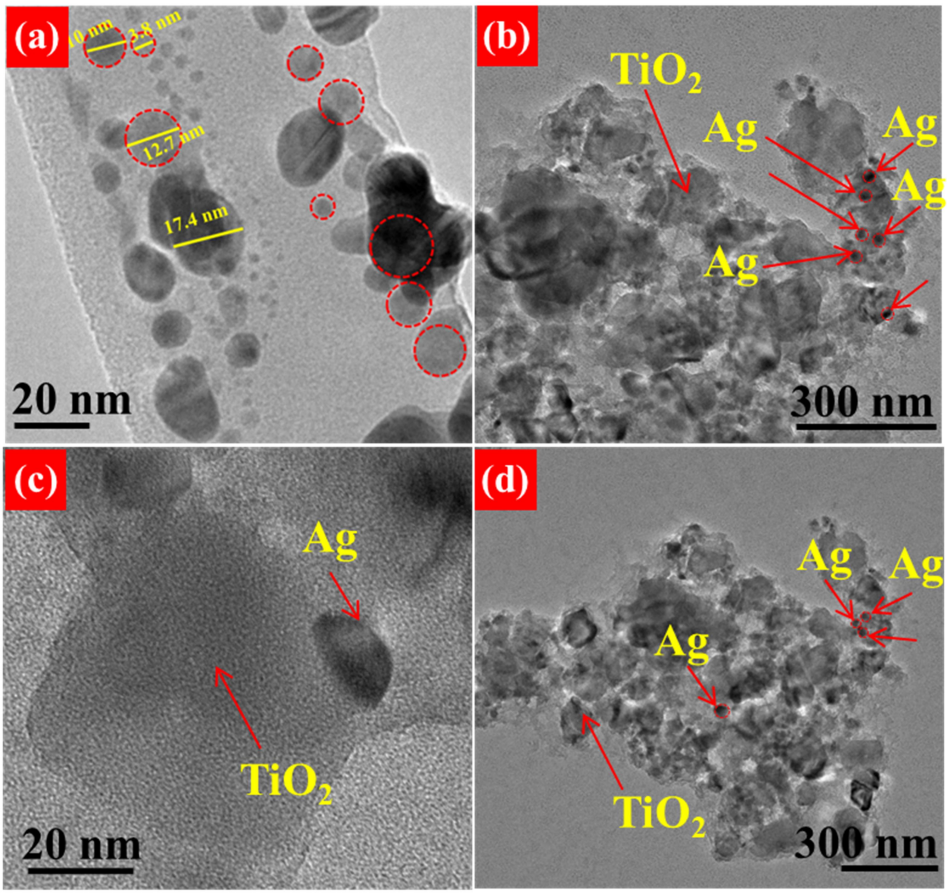

Figure 6.14. TEM images of (a) Ag(S), (b-d) Ag@TiO_2(S).

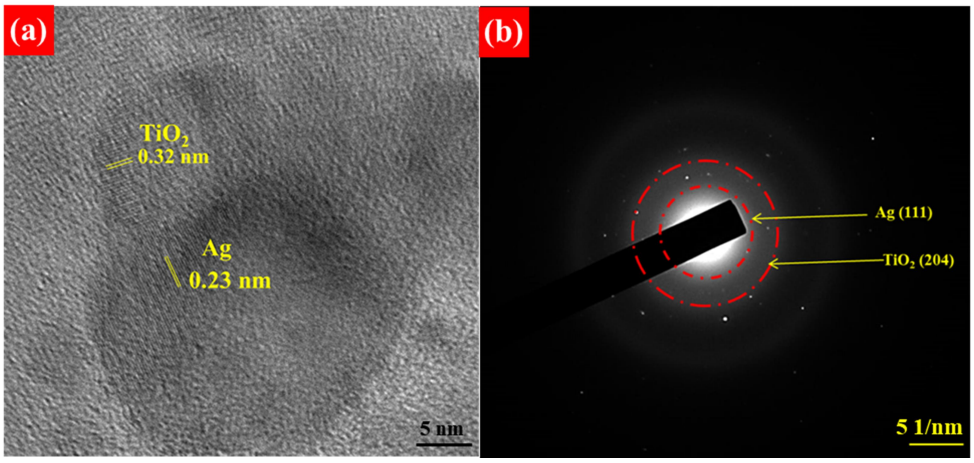

Figure 6.15. (a) HRTEM image and (b) SAED pattern of Ag@TiO_2(S).

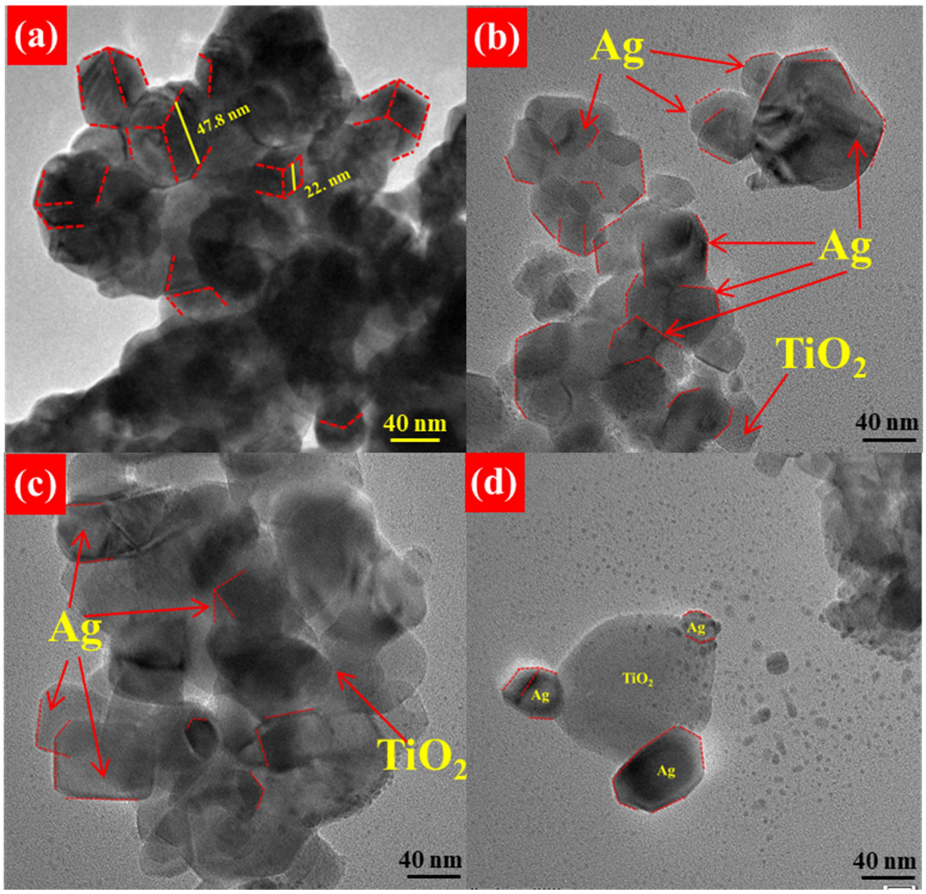

Figure 6.16. TEM images of (a) Ag(C) and (b-d) Ag@TiO_2(C).

Figure 6.16(d) shows a highly detailed TEM image showing Ag nanoparticles with facets surrounding TiO_2. The formation of Ag and TiO_2 phases in Ag@TiO_2(C) was confirmed by the HRTEM images and SAED pattern presented in Figure 6.17(a-d). An interplanar spacing of 0.23 nm, corresponding to the (111) plane of metallic Ag, was measured precisely at the locations of the cubical particles, which are characterized by their well-defined sharp edges, as shown in Figures 6.17(a) and 6.17(c). Again, an interplanar spacing of 0.32 nm was detected in regions devoid of cubical particles, clearly indicating the presence of rutile TiO_2, as shown in Figure 6.17(b). Additionally, the SAED pattern in Figure 6.17(d) reveals two diffraction rings corresponding to the (111) plane of Ag and the (204) plane of anatase TiO_2, further supporting the successful formation of Ag@TiO_2(C). The successful incorporation of bulbous branched Ag

nanostructures into the TiO_2 matrix was confirmed by SEM and TEM analyses, as shown in Figure 6.18(a-d).

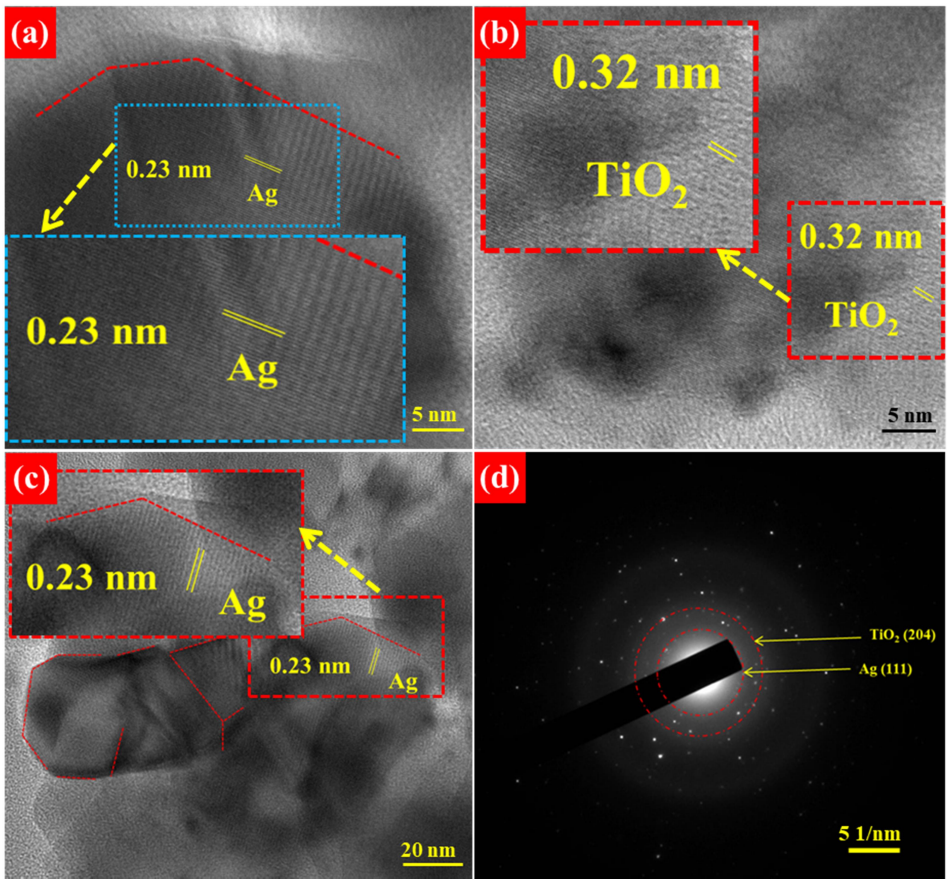

Figure 6.17. (a-c) HRTEM images, and (d) SAED pattern of Ag@TiO_2(C).

The FESEM images of the branched Ag nanostructures (Ag(B)) are presented in Figures 6.18(a) and 6.18(b), clearly revealing their distinctive morphology. A similar structural feature was observed in the TEM image, shown in Figure 6.18(c), where the branched morphology is outlined with a red dashed line for clarity. Size analysis from the SEM images indicates that individual Ag(B) nanoparticles exhibit dimensions in the range of approximately 100-400 nm. Figure 6.18(d) presents the TEM image of Ag@TiO_2(B) calcined at 600 ºC, showing the retention of branched Ag morphology, outlined with a red dashed line. The measured size (100-200 nm) matches that of the separately synthesized Ag structures. Interplanar spacings of 0.22 nm and 0.32 nm, shown in Figures 6.19(a-c), confirm the presence of metallic Ag and rutile TiO_2,

respectively. The SAED pattern in Figure 6.19(d) further supports this, revealing diffraction rings for Ag (111) and TiO_2 (204).

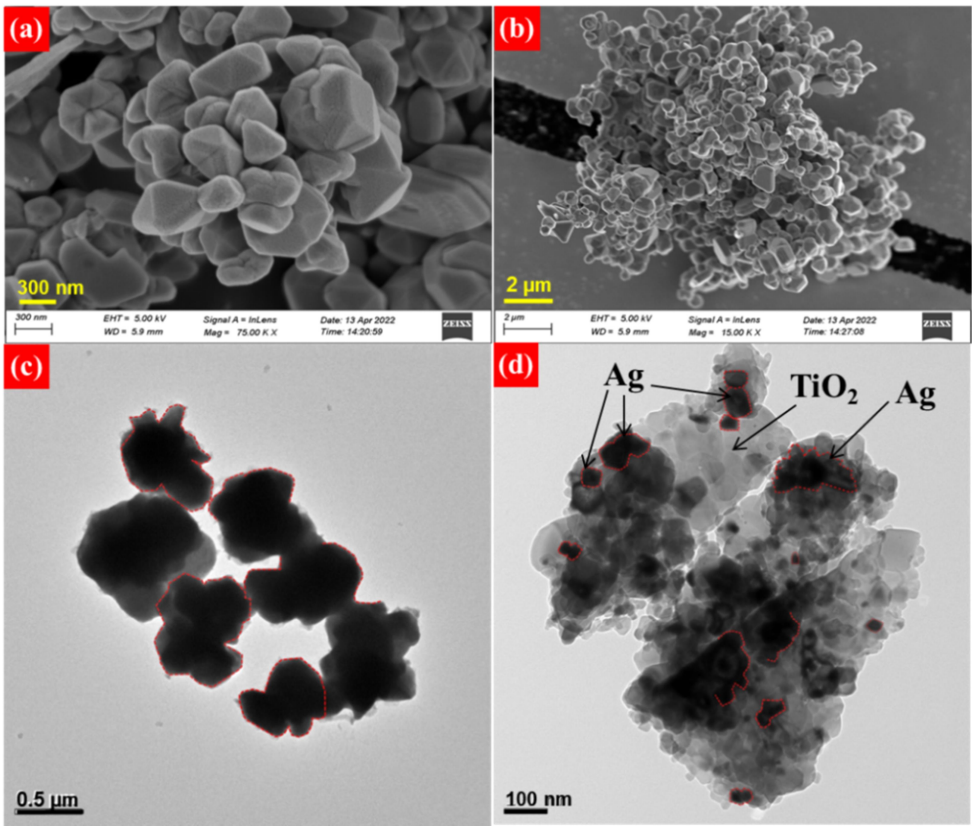

Figure 6.18. (a-b) FESEM, (c) TEM image of Ag(B), and (d) TEM image of Ag@TiO_2(B).

The SEM images of Ag@TiO_2(C) prepared with different Ag concentrations, along with Ag@TiO_2(S), are presented in Figure 6.20(a-f). Notably, the calcined photocatalysts exhibit significantly larger particle sizes compared to their raw, non-calcined counterparts. Ag@TiO_2 photocatalysts synthesized with 10 mL of spherical and cubical Ag and calcined at 600 ºC are shown in Figures 6.20(a) and 6.20(d), respectively. The pre-calcined forms of Ag@TiO_2(C) with 20 mL and 5 mL Ag loadings are displayed in Figures 6.20(c) and 6.20(f), while their corresponding calcined forms appear in Figures 6.20(b) and 6.20(e). Figure 6.21(a-d) shows SEM images of the best-performing Ag@TiO_2(C) photocatalyst, synthesized using 10 mL of cubical Ag and

calcined at 600 ºC, under various magnifications. A uniform distribution of cubical-shaped particles are visible, particularly in Figures 6.21(c) and 6.21(d).

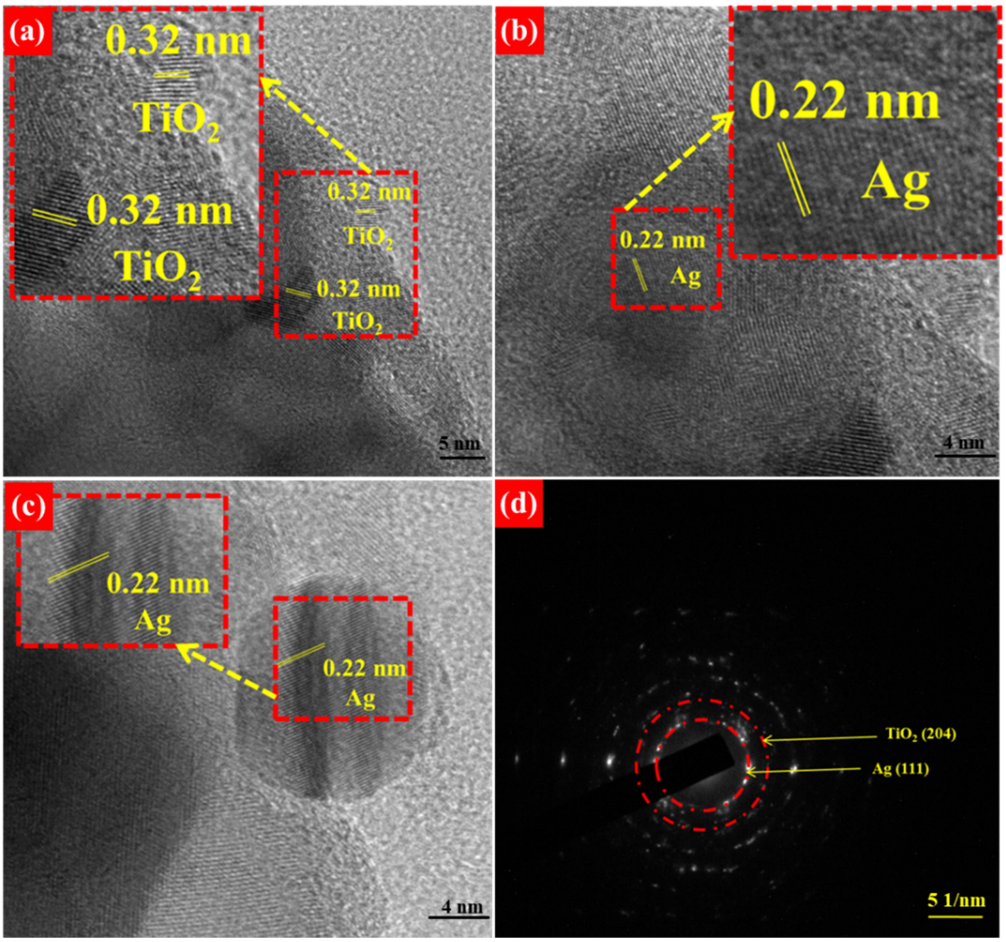

Figure 6.19. (a-c) HRTEM images and (d) SAED pattern of Ag@TiO_2(B).

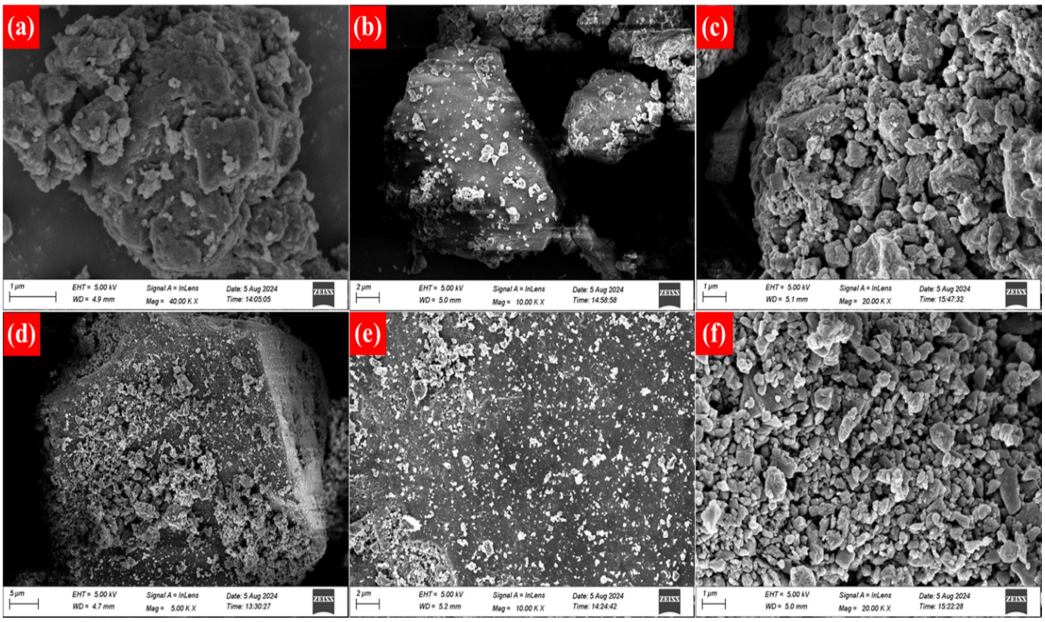

Figure 6.20. SEM images of (a) Ag@TiO_2(S), (b) Ag@TiO_2(C20), (c) raw Ag@TiO_2(C20), (d) Ag@TiO_2(C10), (e) Ag@TiO_2(C5), and (f) raw Ag@TiO_2(C5).

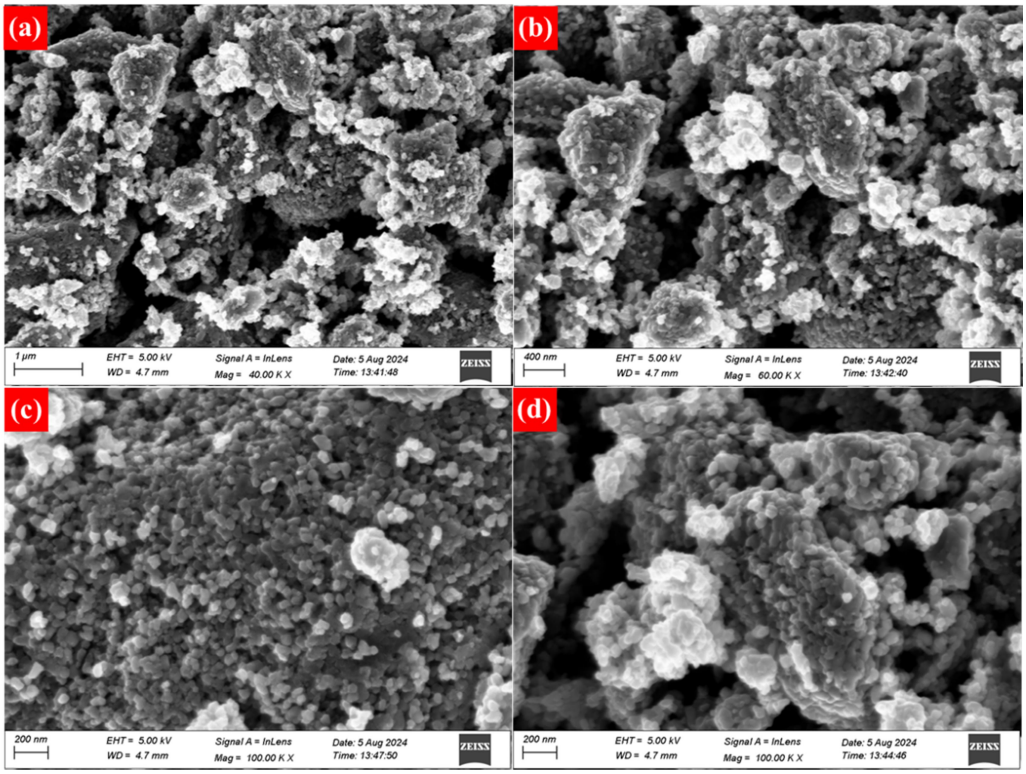

Figure 6.21. (a-d) SEM images of Ag@TiO_2(C10) at different magnifications.

6.3.4. Raman and photoluminescence analysis

The Raman spectra of TiO_2, Ag@TiO_2(C), Ag@TiO_2(S), and Ag@TiO_2(B) calcined at 600 ºC, are presented in Figure 6.22. Characteristic peaks corresponding to the rutile phase are observed at 140 cm^{-1}, 233 cm^{-1}, 444 cm^{-1}, and 609 cm^{-1}, while peaks at 144 cm^{-1} and 516 cm^{-1} correspond to the anatase phase [13-16]. Both TiO_2 and Ag@TiO_2(C) are observed to be rutile-dominat exhibiting the rutile peak at 140 cm^{-1}, attributed to the symmetric B_{1g} mode. In contrast, Ag@TiO_2(S) and Ag@TiO_2(B) display anatase peaks at 144 cm^{-1} (E_g) and 516 cm^{-1} (A_{1g}+B_{1g}), confirming their anatase phase composition, which is consistent with XRD results. Notably, all samples TiO_2, Ag@TiO_2(C), Ag@TiO_2(S), and Ag@TiO_2(B) show peaks at 444 cm^{-1} and 609 cm^{-1}, corresponding to the E_g and A_{1g} modes of the rutile phase.

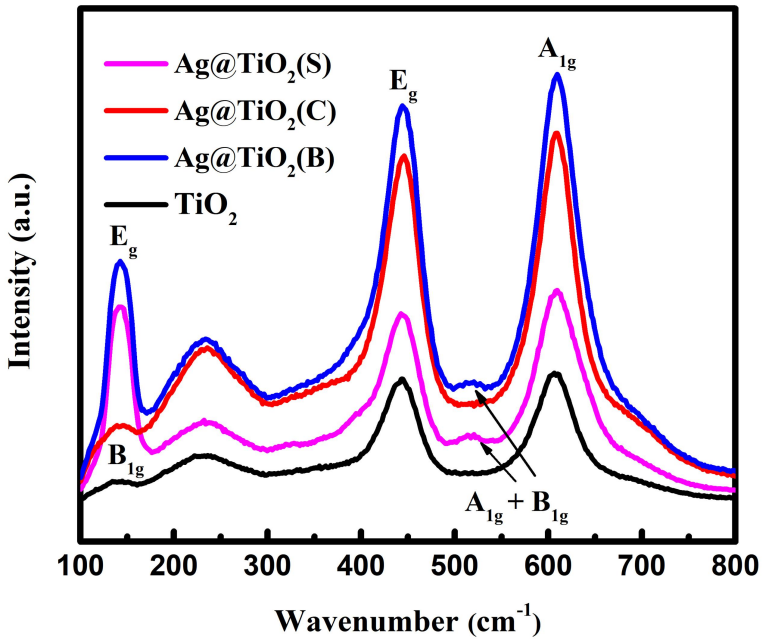

Figure 6.22. Raman spectra of Ag@TiO_2 (prepared with different Ag shapes) and pristine TiO_2 calcined at 600 ºC.

A distinct broad peak around 233 cm^{-1} was also observed in all the photocatalysts, which is attributed to two-phonon scattering in the rutile phase [15]. This peak appears more intense in Ag@TiO_2(C) and Ag@TiO_2(B) compared to TiO_2 and Ag@TiO_2(S). The enhanced intensity in Ag@TiO_2(C) and Ag@TiO_2(B) may be attributed to the larger size and anisotropic shapes (cubical and bulbous) of Ag, which promote stronger

Raman scattering. Alternatively, it could result from a higher Ag loading in these samples relative to Ag@TiO_2(S).

The photoluminescence spectra of TiO_2, Ag@TiO_2(C), Ag@TiO_2(S), and Ag@TiO_2(B) calcined at 600 ºC, are shown in Figure 6.23. The PL spectra span a broad wavelength range from 400 to 550 nm, and are influenced by various factors, including self-trapped excitons, oxygen vacancies, and surface states [17]. The emission peak around 419 nm, which slightly varies among the samples due to their differing bandgaps, corresponds to band-edge emission related to the corresponding bandgap [18]. Peaks at approximately 439 nm and 469 nm are attributed to intrinsic structural defects and surface oxygen vacancies, respectively [17]. Additionally, the emission at 450 nm has been reported to originate from self-trapped excitons within the TiO_6 octahedra [19]. The PL spectra reveal lower PL intensities for all Ag@TiO_2 photocatalysts compared to pure TiO_2, indicating reduced charge carrier recombination. This reduction in the PL intensity in all the Ag@TiO_2 samples can be attributed to the formation of a Schottky junction between metallic Ag and TiO_2, where the resulting internal electric field promotes efficient charge separation. The extent of PL intensity reduction varies among the Ag@TiO_2 samples, suggesting that the size and shape of the Ag nanoparticles plays a significant role in influencing recombination dynamics. It was observed that Ag@TiO_2(C) shows higher PL intensity than both Ag@TiO_2 (S) and Ag@TiO_2(B). TEM analysis confirms that the cubical Ag particles are larger than the spherical ones but smaller than the bulbous branched particles. Since smaller Ag nanoparticles are generally reported to exhibit stronger PL emissions, the comparatively higher PL intensities of Ag@TiO_2(S) and Ag@TiO_2(C) relative to Ag@TiO_2(B) can be reasonably attributed to their smaller particle sizes. However, the observation that Ag@TiO_2(C) has a higher PL intensity than Ag@TiO_2(S) appears contradictory if only particle size is considered. This discrepancy can be explained by considering plasmonic effects. The cubical Ag nanostructures in Ag@TiO_2(C) can generate stronger localized electromagnetic fields than the spherical (Ag@TiO_2(S)) or bulbous (Ag@TiO_2(B)) counterparts, owing to their optimal shape and size. This field enhancement can significantly boost electron-hole pair generation in TiO_2 [20]. If a portion of these photogenerated carriers are not effectively separated and instead undergo radiative recombination, it could lead to higher PL emission despite the overall improved

photocatalytic activity, consistent with the observed result. The enhanced PL intensity in Ag@TiO_2(C) may also arise from radiative plasmon decay, contributing to metal-enhanced luminescence [21].

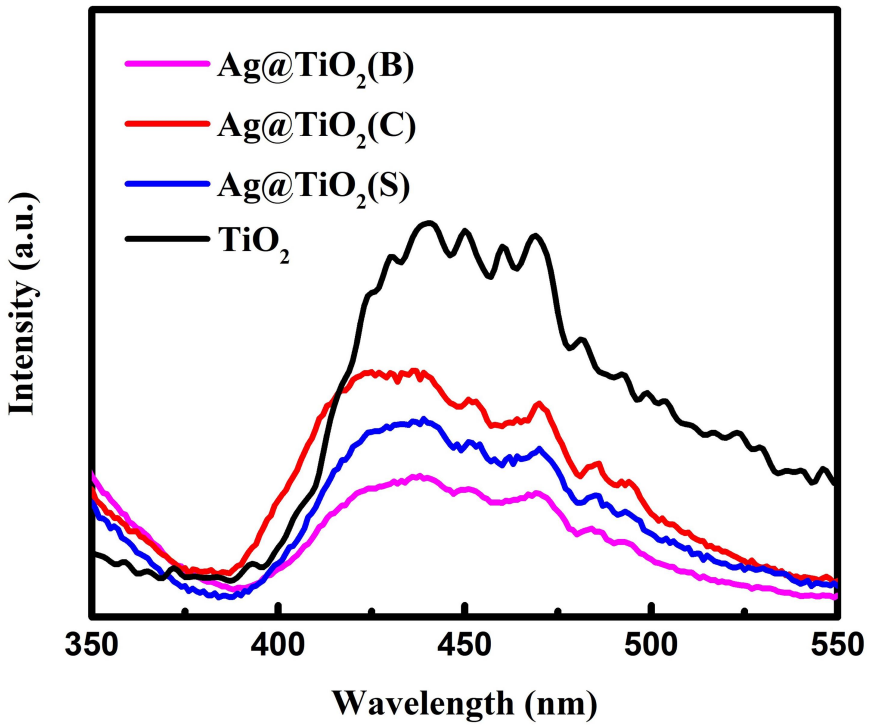

Figure 6.23. Photoluminescence spectra of Ag@TiO_2 (prepared with different Ag shapes) and pristine TiO_2 calcined at 600 ºC.

6.3.5. XPS analysis

X-ray photoelectron spectroscopy (XPS) was employed to investigate the chemical composition and electronic structure of the optimized Ag@TiO_2(C) photocatalyst. The survey spectrum, presented in Figure 6.24(a), confirms the presence of Ag, Ti, O, and C elements. The high-resolution Ti 2p spectrum in Figure 6.24(b) displays two prominent peaks at binding energies of 458.5 eV and 464.3 eV, corresponding to Ti ($2p_{1/2}$) and Ti ($2p_{3/2}$), respectively, which are characteristic of Ti^{4+} oxidation state [22-24]. Figure 6.24(c) shows the O 1s core-level spectrum, where peaks at 529.7 eV and 531.0 eV are attributed to lattice oxygen and surface-adsorbed hydroxyl species, respectively [25-27]. Additionally, the Ag 3d spectrum in Figure 6.24(d) exhibits two distinct peaks at 368 eV ($3d_{5/2}$) and 374 eV ($3d_{3/2}$) separated by 6.0 eV due to spin–orbit coupling, indicating the presence of metallic silver [28-30].

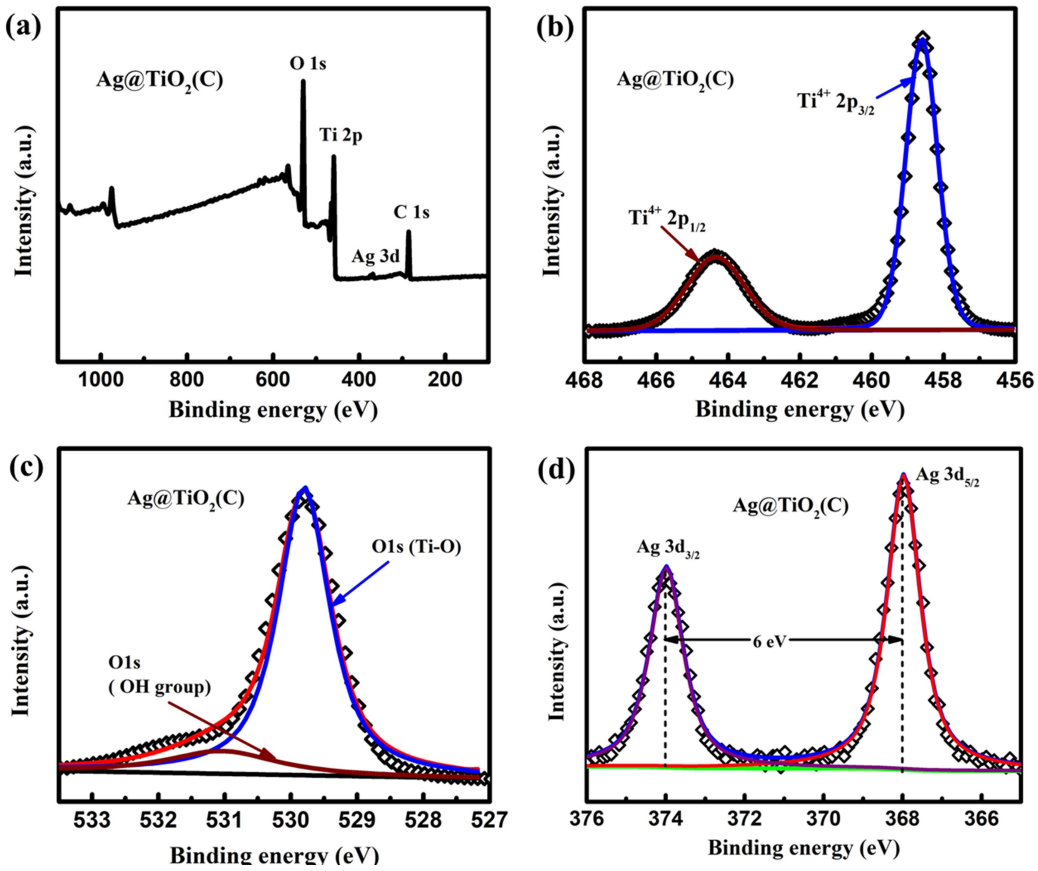

Figure 6.24. (a) XPS survey profile of Ag@TiO_2(C), XPS peak fit of Ag@TiO_2(C): (b) Ti 2p spectra, (c) O 1s, and (d) Ag 3d.

6.4. Summary

Out of all the Ag@TiO_2 photocatalysts prepared with different Ag shapes, the cubical Ag loaded TiO_2 calcined at 600 ºC shows the highest photocatalytic performance against degradation of MB under visible light. The superior performance of this photocatalyst can be ascribed to the suitable size and cubical shape of Ag nanoparticles. The size of the cubical Ag (Ag(C)) was found to be between 20-70 nm which is larger than that of spherical Ag (Ag(S)) but smaller than that of branched Ag nanoparticles (Ag(B)). Moreover, the shape of a cube offers two different plasmonic resonances, while sphere exhibits only a single resonance peak. The UV-vis absorbance spectra of Ag(C) also showed that one of its characteristic resonance peaks (at 288 nm), lies in a short wavelength region, which implies that Ag(C) can inject plasmonic electrons, with energy higher than what is possible in Ag(S), through DET to conduction band of TiO_2

in Ag@TiO_2(C), when the resonance at this shorter wavelength is excited. This could be also one of the reasons for higher emission in PL spectra of Ag@TiO_2(C). The cubical shape of the Ag(C) also offers facets and edges to create an enhanced local electric field in the vicinity of the nanoparticle. This highly intense near field can then boost the charge carrier generation in the conduction band of TiO_2. In comparison, the spherical Ag nanoparticles of Ag(S) are smaller in size, and consequently shows a resonance peak at shorter wavelength (390 nm) than the main resonance peak (at 417 nm) of Ag(C). However, the absorbance spectrum of Ag(S) exhibits a confined peak within a narrow wavelength range, indicating relatively lower responsiveness than that of Ag(C) in the visible light region. As a result, Ag@TiO_2(S) shows second highest enhanced activity owing to its own intense LSPR and efficient hot electron injection. The smaller size of Ag(S) also generates strong local-fields, while cubical Ag in Ag@TiO_2(C), with sharp edges, induces even stronger fields. On the other hand, the sizes of bulbous branched nanostructures are larger, in the size range of 100-200 nm, and thus show broad absorbance in the visible light range. However, due to less distinct resonances and the bigger size of the particles, the plasmonic benefit of this branched Ag to the host TiO_2 could be less pronounced. Thus, the optimized shape of Ag for Ag@TiO_2 photocatalysts was found to be cubical shape. Thereafter, the loading amount of Ag(C) solution was varied to determine the optimum amount. The photocatalytic evaluation experiments revealed that the 10 mL Ag loading, to form Ag@TiO_2(C10), was the optimum amount among other chosen amounts concentrations. It is apparent that Ag@TiO_2(C5) possess lower Ag concentration, so that it only benefits from plasmonic effects of the available Ag nanoparticles and thus exhibits lower activity. On the other hand, Ag@TiO_2(C20) with higher Ag concentration suffers from recombination issues caused by Ag nanoparticles acting as recombination centers. Thus, Ag@TiO_2(C10) photocatalyst was found to exhibit superior performance with optimized Ag shape and loading. The calcination temperature of Ag@TiO_2(C10) was further varied, and photocatalytic performance of each of these variants were evaluated. The result indicated that 600 ºC was the optimal condition for Ag@TiO_2(C10). Finally, all the shape and loading variants of Ag@TiO_2 photocatalyst were thermally treated to transform them into the rutile phase, and upon evaluating their photoactivity, the cubical Ag loaded TiO_2 with 10 mL Ag i.e Ag@TiO_2(C10) emerged as the most efficient photocatalyst.

References:

1. W.A. Murray, W.L. Barnes, Plasmonic materials, Adv. Mater. 19 (2007) 3771-3782.
2. B.J. Wiley, S.H. Im, Z.Y. Li, J. McLellan, A. Siekkinen, Y. Xia, Maneuvering the surface plasmon resonance of silver nanostructures through shape-controlled synthesis, J. Phys. Chem. B 110 (2006) 15666–15675.
3. M. Rycenga, C.M. Cobley, J. Zeng, W. Li, C.H. Moran, Q. Zhang, D. Qin, Y. Xia, Controlling the synthesis and assembly of silver nanostructures for plasmonic applications, Chem. Rev. 111 (2011) 3669-3712.
4. C.L. Nehl, J.H. Hafner, Shape-dependent plasmon resonances of gold nanoparticles, J. Mater. Chem. 18 (2008) 2415-2419.
5. H. Xiang, X. Zhang, D. Neuhauser, G. Lu, Size-dependent plasmonic resonances from large-scale quantum simulations, J. Phys. Chem. Lett. 5 (2014) 1163-1169.
6. C.M. Cobley, M. Rycenga, F. Zhou, Z.Y. Li, Y. Xia, Controlled etching as a route to high quality silver nanospheres for optical studies, J. Phys. Chem. C 113 (2009) 16975-16982.
7. J.J. Mock, M. Barbic, D.R. Smith, D.A. Schultz, S. Schultz, Shape effects in plasmon resonance of individual colloidal silver nanoparticles, J. Chem. Phys. 116 (2002) 6755-6759.
8. V. Juvé, M.F. Cardinal, A. Lombardi, A. Crut, P. Maioli, J. Pérez-Juste, L.M. Liz-Marzán, N. Del Fatti, F. Vallée, Size-dependent surface plasmon resonance broadening in nonspherical nanoparticles: single gold nanorods, Nano Lett. 13 (2013) 2234-2240.
9. K.L. Kelly, E. Coronado, L.L. Zhao, G.C. Schatz, The optical properties of metal nanoparticles: the influence of size, shape, and dielectric environment, J. Phys. Chem. B 107 (2003) 668-677.
10. J. Zeng, S. Roberts, Y. Xia, Nanocrystal-based time–temperature indicators, Chem. Eur. J. 16 (2010) 12559-12563.
11. S.K. Cushing, J. Li, F. Meng, T.R. Senty, S. Suri, M. Zhi, M. Li, A.D. Bristow, N. Wu, Photocatalytic activity enhanced by plasmonic resonant energy transfer from metal to semiconductor, J. Am. Chem. Soc. 134 (2012) 15033-15041.
12. C. Clavero, Plasmon-induced hot-electron generation at nanoparticle/metal-oxide

interfaces for photovoltaic and photocatalytic devices, Nat. Photonics 8 (2014) 95-103.

13. B.R. Bade, S. Rondiya, S.R. Bhopale, N.Y. Dzade, M.M. Kamble, A. Rokade, M.P. Nasane, M.A. More, S.R. Jadkar, A.M. Funde, Investigation of growth mechanism for highly oriented TiO_2 nanorods: the role of reaction time and annealing temperature, SN Appl. Sci. 1 (2019) 1-13.
14. S. Challagulla, K. Tarafder, R. Ganesan, S. Roy, Structure sensitive photocatalytic reduction of nitroarenes over TiO_2, Sci. Rep. 7 (2017) 1-11.
15. J. Singh, K. Sahu, S. Mohapatra, Thermal annealing induced evolution of morphological, structural, optical and photocatalytic properties of Ag-TiO_2 nanocomposite thin films, J. Phys. Chem. Solid. 129 (2019) 317-323.
16. L. Palliyaguru, U.S. Kulathunga, L.I. Jayarathna, C.D. Jayaweera, P.M. Jayaweera, A simple and novel synthetic route to prepare anatase TiO_2 nanopowders from natural ilmenite via the H_3PO_4/NH_3 process, Int. J. Miner. Metall. Mater. 27 (2020) 846-855.
17. T. Dhandayuthapani, R. Sivakumar, R. Ilangovan, Growth of micro flower rutile TiO_2 films by chemical bath deposition technique: study on the properties of structural, surface morphological, vibrational, optical and compositional, Surface. Interfac. 4 (2016) 59-68.
18. G. Nabi, W. Raza, M.B. Tahir, Green synthesis of TiO_2 nanoparticle using cinnamon powder extract and the study of optical properties, J. Inorg. Organomet. Polym. Mater. 30 (2020) 1425-1429.
19. V. Kumaravel, S. Rhatigan, S. Mathew, M.C. Michel, J. Bartlett, M. Nolan, S.C. Pillai, Mo doped TiO_2: impact on oxygen vacancies, anatase phase stability and photocatalytic activity, J. Phys. Materials 3 (2020) 025008.
20. Z. Lou, Z. Wang, B. Huang, Y. Dai, Synthesis and activity of plasmonic photocatalysts, ChemCatChem 6 (2014) 2456-2476.
21. O.A. Yeshchenko, I.M. Dmitruk, A.A. Alexeenko, M.Y. Losytskyy, A.V. Kotko, A.O. Pinchuk, Size-dependent surface-plasmon-enhanced photoluminescence from silver nanoparticles embedded in silica, Phys. Rev. B 79 (2009) 235438.
22. B. Bharti, S. Kumar, H.N. Lee, R. Kumar, R. Formation of oxygen vacancies and Ti^{3+} state in TiO_2 thin film and enhanced optical properties by air plasma

treatment, Sci. Rep. 6 (2016) 32355.

23. C. Yu, D. Cai, K. Yang, C.Y. Jimmy, Y. Zhou, C. Fan, Sol-gel derived S, I-codoped mesoporous TiO_2 photocatalyst with high visible-light photocatalytic activity, J. Phys. Chem. Solids 71 (2010) 1337-1343.
24. F. Peng, L. Cai, L. Huang, H. Yu, H. Wang, Preparation of nitrogen-doped titanium dioxide with visible-light photocatalytic activity using a facile hydrothermal method, J. Phys. Chem. Solids 69 (2008) 1657-1664.
25. X. Zhang, L. Wang, C. Liu, Y. Ding, S. Zhang, Y. Zeng, Y. Liu, S. Luo, A bamboo-inspired hierarchical nanoarchitecture of Ag/CuO/TiO_2 nanotube array for highly photocatalytic degradation of 2, 4-dinitrophenol, J. Hazard. Mater. 313 (2016) 244-252.
26. G. Wang, Z. Fu, T. Wang, W. Lei, P. Sun, Y. Sui, B. Zou, A rational design of hollow nanocages Ag@CuO-TiO_2 for enhanced acetone sensing performance, Sens. Actuators B Chem. 295 (2019) 70-78.
27. D.A. Svintsitskiy, T.Y. Kardash, A.I. Boronin, Surface dynamics of mixed silver-copper oxide $AgCuO_2$ during X-ray photoelectron spectroscopy study, Appl. Surf. Sci. 463 (2019) 300-309.
28. X. You, F. Chen, J. Zhang, M. Anpo, A novel deposition precipitation method for preparation of Ag-loaded titanium dioxide, Catal. Lett., 102 (2005) 247-250.
29. H. Zhang, C. Liang, J. Liu, Z. Tian, G. Wang, W. Cai, Defect-mediated formation of Ag cluster-doped TiO_2 nanoparticles for efficient photodegradation of pentachlorophenol, Langmuir 28 (2012) 3938-3944.
30. S.K. Pandey, M.K. Tripathi, V. Ramanathan, P.K. Mishra, D. Tiwary, Highly facile Ag/NiO nanocomposite synthesized by sol-gel method for mineralization of rhodamine B, J. Phys. Chem. Solids 159 (2021) 110287.